Magnetic Field Structure and Faraday Rotation of the Plerionic Supernova Remnant G21.5–0.9

Paul C. W. Lai[1] , C.-Y. Ng[1] , and Niccolo' Bucciantini[2,3,4]
[1] Department of Physics, The University of Hong Kong, Pokfulam Road, Hong Kong; paullai@connect.hku.hk
[2] INAF—Osservatorio Astrofisico di Arcetri, Largo E. Fermi 5, I-50125 Firenze, Italy
[3] INFN—Sezione di Firenze, Via G. Sansone 1, I-50019 Sesto F. no (Firenze), Italy
[4] Dipartimento di Fisica e Astronomia, Università degli Studi di Firenze, Via G. Sansone 1, I-50019 Sesto F. no (Firenze), Italy
Received 2021 September 6; revised 2022 April 1; accepted 2022 April 2; published 2022 April 28

Abstract

We present a polarimetric study of the pulsar wind nebula (PWN) in supernova remnant G21.5−0.9, using archival Very Large Array data taken at 5 and 7.4 GHz. The rotation measure (RM) map of the PWN shows a symmetric pattern that aligns with the presumed pulsar spin axis direction, implying a significant contribution to the RM from the nebula. We suggest that the spatial variation of the internal RM is mostly caused by the nonuniform distribution of electrons originating from the supernova ejecta. Our high-resolution radio polarization map reveals a global radial *B*-field. We show that a simple model with overall radial field and turbulence on a small scale can reproduce many observed features of the PWN, including the polarization pattern and polarized fraction. The modeling results also reject a strong large-scale toroidal *B*-field, suggesting that the toroidal field observed in the inner PWN cannot propagate to the entire nebula. Lastly, our model predicts that the internal Faraday rotation would break the linear relation between the polarization angle and the square of the wavelength, and cause severe depolarization at low frequencies.

Unified Astronomy Thesaurus concepts: Supernova remnants (1667); Radio interferometry (1346); Polarimetry (1278); Magnetic fields (994); Pulsars (1306)

1. Introduction

A pulsar carries a strong magnetic field and rotates very rapidly. It acts as a rotating magnetic dipole, generating a strong electric potential that accelerates electrons and positrons to relativistic speeds. The relativistic particles launched from the pulsar, together with the electromagnetic Poyting flux, are known as pulsar wind. Upon crushing into its surroundings, e.g., supernova (SN) ejecta, it creates a termination shock (TS). The shock accelerates the particles and randomizes their motion, resulting in synchrotron radiation. Such a synchrotron bubble surrounding the pulsar is called a pulsar wind nebula (PWN). Shock acceleration and magnetic reconnection play an important role in accelerating pulsar wind particles (Amato 2020). It is found that many young pulsars have X-ray tori/rings around them (see Ng & Romani 2004, 2008). These correspond to the pulsar wind TS location, and the shape is caused by latitude-dependent pulsar wind (Bogovalov & Khangoulyan 2002).

Force-free pulsar magnetosphere solutions suggest that the magnetic field is toroidal close to the pulsar light cylinder (Contopoulos et al. 1999), and this is believed to hold true before the pulsar wind reaches the TS. Theoretical work has not yet been able to describe the postshock magnetic structure in the full body of the nebula. Observationally, young PWNe show large diversity in the global magnetic field configuration. For example, Vela has a toroidal field (Dodson et al. 2003) and 3C58 has a *B*-field parallel to its pulsar spin axis (Reich 2002). The magnetic field structures of G18.95−1.1 and G328.4+0.2 look similar to 3C58 (Reich 2002; Johnston et al. 2004), but the directions of their pulsar spin axes have not yet been identified. G21.5−0.9 (Becker & Szymkowiak 1981; Reich 2002) and DA 495 (Kothes et al. 2008) have

large-scale radial magnetic fields, while the Crab Nebula has a radial field only near its boundary (Bietenholz & Kronberg 1990). Both G21.5−0.9 and the Crab show toroidal fields close to the TS, as theories predicted (Zajczyk et al. 2012; Moran et al. 2013). Some other PWNe simply have disordered *B*-fields, as in G292.0+1.8 (Gaensler & Wallace 2003).

G21.5−0.9 is a composite supernova remnant (SNR) consisting of a PWN core surrounded by an SNR shell. Both the PWN and the shell are highly spherical, with angular diameters of 80″ and 5′, respectively (Matheson & Safi-Harb 2010). At the center of the SNR there is a radio pulsar, J1833−1034, powering the PWN (Gupta et al. 2005; Camilo et al. 2006). It has a spin period $P = 62$ ms, a spin-down rate $\dot{P} = 2.0 \times 10^{-13}$, surface magnetic field strength $B = 3.6 \times 10^{12}$ G, and spin-down luminosity $\dot{E} = 3.3 \times 10^{37}$ erg s^{-1} (Camilo et al. 2006).

By measuring the expansion speed of G21.5−0.9, its age has been found to be 870 yr (Bietenholz & Bartel 2008). This makes G21.5−0.9 the second youngest known PWN in the galaxy, only after Kes 75 (Reynolds et al. 2018). CO and H I absorption measurements suggest a distance of 4.7 ± 0.4 kpc (Camilo et al. 2006).

Surrounding the pulsar is compact X-ray emission of radius ~3″–6″, which corresponds to the TS (Guest et al. 2019), and it has been fit with a torus model to infer the pulsar spin axis orientation (Ng & Romani 2008; see also Figure 1). In radio, a high-resolution Very Large Array (VLA) study revealed the filamentary structure of the PWN (Bietenholz & Bartel 2008). Different spectral indexes of G21.5−0.9 have been reported at around 5 GHz, from $\alpha = -0.08^{+0.09}_{-0.06}$ ($S_\nu \propto \nu^{-\alpha}$) to $+0.06 \pm 0.03$ to $+0.12 \pm 0.03$ (Bietenholz & Bartel 2008; Bhatnagar et al. 2011; Sun et al. 2011).[5]

---

[5] In Bhatnagar et al. (2011), the sign of the spectral index reported in the text is different from that in Figure 1. Through private communication, we have confirmed that the text has a typo and the image shows the correct spectral index.
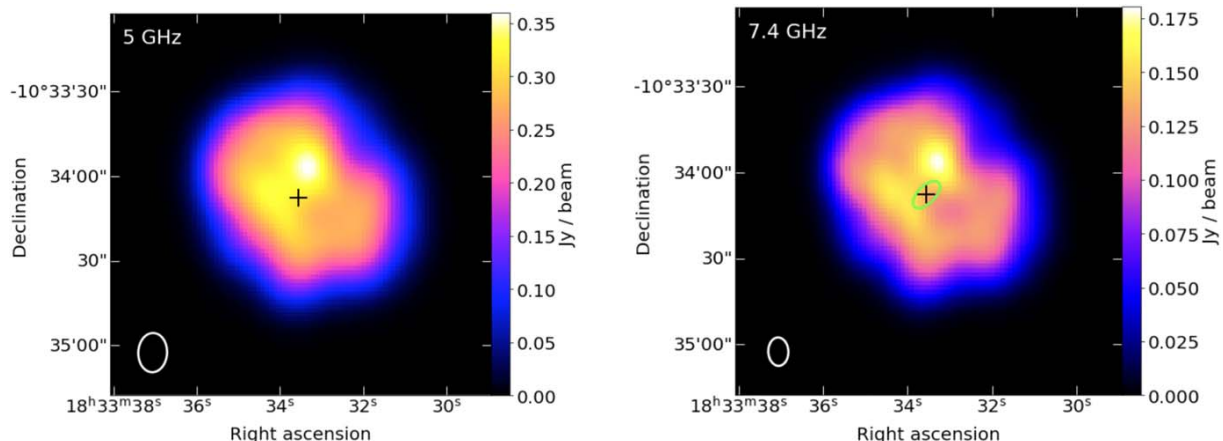
Figure 1. Left: total intensity map of G21.5−0.9 at 5 GHz. The beam size is $13\rlap{.}{''}9 \times 10\rlap{.}{''}2$. The rms noise is 0.09 mJy beam^{-1}. Right: the same plot at 7.4 GHz. The position and orientation of the X-ray torus is indicated by the green ellipse (not in scale; Ng & Romani 2008). The beam size is $9\rlap{.}{''}9 \times 7\rlap{.}{''}0$ and the rms noise is 0.07 mJy beam^{-1}. In both panels, the cross marks the position of PSR J1833−1034, and the beam size is indicated at the lower left.

The first radio polarimetric observation of G21.5−0.9 was performed over 40 years ago (Becker & Szymkowiak 1981), and it revealed a radial magnetic field structure. The study, however, did not investigate the detailed distribution of the Faraday rotation in the source. Later polarimetric studies were only done at higher frequencies, for which the Faraday effect is negligible (Reich 2002). In this study, we derive the rotation measure (RM) toward G21.5−0.9 and map the intrinsic *B*-field orientation at high resolution, using archival VLA data. The observation details and imaging methods are described in Section 2, and the results are presented in Section 3. We discuss the observed features in Section 4. In Section 5, we show that a turbulent radial magnetic field model is able to reproduce the observed features. We summarize our findings in Section 6.

2. Observations and Data Reduction

We analyzed an archival VLA observation of G21.5−0.9 taken on 2010 August 12 in the C-array configuration. These are the data that have the highest resolution with full Stokes parameters recorded. The data were previously used to study the radio morphology and spectrum of the source, but no polarization property of the source was reported (Bhatnagar et al. 2011). The observation parameters are listed in Table 1. The observations were done in the C band, and were divided into two separate frequency bands centering at 5 and 7.4 GHz, with a bandwidth of 1.024 GHz each. The observations have *u–v* coverage that is sensitive to scales from $10''$ to $5'$. This well covers the PWN size of $80''$. The data were taken in the continuum mode, with two hours of total on-source time spanning seven hours. J1331+3030 was observed as a flux and polarization angle (PA) calibrator. J1822−0938 was observed at 20 minute intervals to determine the complex gain and leakage terms.

We used Common Astronomical Software Application version 5.6 for all the data reduction (McMullin et al. 2007). Calibrations were done manually, because the data are too old to run the current pipeline. We first applied the necessary flaggings, including edge channels, shadowed antennas, zero-amplitude data, etc. Then we identified and flagged the radio frequency interference using the task `rflag`. Next, the flux, bandpass, gain, and polarization calibration solutions were determined using the two calibrators

Table 1
Observational Parameters

Observing date	2010 August 12
VLA configuration	C
Number of antennas	23
Baseline	30–1030 m
u–v coverage	0.45–19 kλ, 0.69–27 kλ
Center freq. (GHz)	5, 7.4
Bandwidth (GHz)	1.024, 1.024
Channel width (MHz)	2
On-source time (min)	115

mentioned above. Finally, we employed self-calibration to boost the signal-to-noise ratio (S/N). The dynamic range was nearly doubled after a couple of iterations. We formed Stokes I, Q, and U images, and performed deconvolution using the task `tclean`. To optimize between sensitivity and resolution, we chose the Briggs weighting algorithm with robust = 0 for all images. Since the observations were done in two separate frequency bands, we formed two images at 5 and 7.4 GHz. This is different from the previous study (Bhatnagar et al. 2011), so that we can cross-validate the results. In the final maps, the synthesized beams have FWHMs of $13\rlap{.}{''}9 \times 10\rlap{.}{''}2$ and $9\rlap{.}{''}9 \times 7\rlap{.}{''}0$ at 5 GHz and 7.4 GHz, respectively. The rms noises in the Stokes I image are 90 and 70 μJy beam^{-1} at 5 and 7.4 GHz, respectively, and in the Stokes Q and U images are 50 and 45 μJy beam^{-1} at 5 and 7.4 GHz, respectively. The observed rms noise is similar to the theoretical sensitivity.

The Q and U images are used to produce the linear polarization intensity (PI) and PA maps, where PI $= \sqrt{Q^2 + U^2}$ and PA $= \frac{1}{2}\arctan(U/Q)$. We corrected the Ricean bias in the former (Wardle & Kronberg 1974) using the measured rms noise levels mentioned above. The observed PAs are in general different from the intrinsic ones because of the Faraday rotation. The change in the PA is proportional to the square of the wavelength, as $\Delta\text{PA} = \text{RM}\,\lambda^2$, where λ is the observing wavelength. To solve for the RM, we generated two images at 5 and 7.4 GHz, each with identical resolutions. We first applied a Gaussian taper of $14'' \times 11''$ to the visibility data, then followed the same imaging and cleaning procedures as described above. The final images were
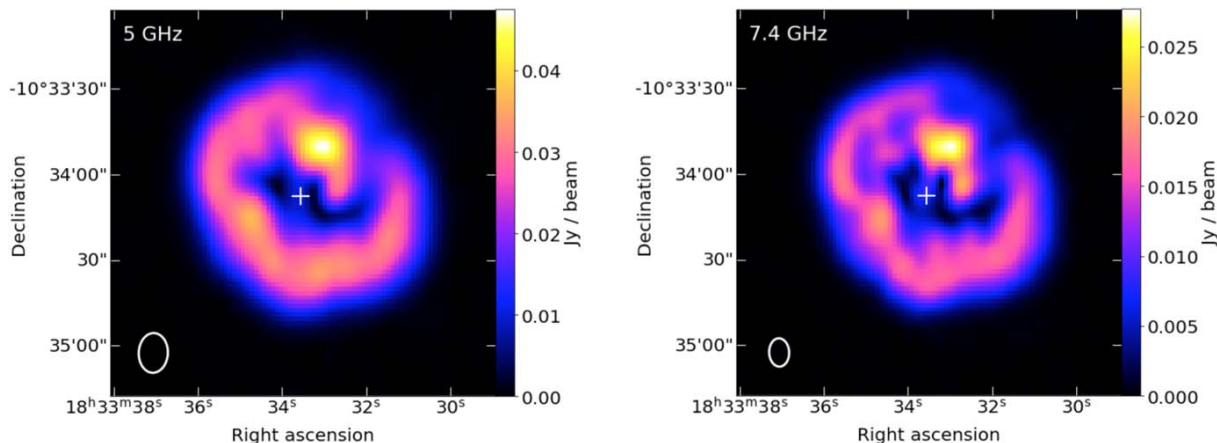
Figure 2. Linear PI maps of G21.5−0.9. The crosses mark the position of PSR J1833−1034. The beam sizes are same as in Figure 1 and are indicated at the lower left.

convolved from the model images by the same beam size as the taper ($14'' \times 11''$). The PA and total intensity maps were then used to solve for the RM and spectral index, respectively. We further divided the data into four frequency bands to confirm that there was no $n\pi$-ambiguity in our case. We used the RM obtained from the two-band result because it has a better S/N. The RM is only calculated for pixels for which the PI is larger than 1 mJy beam^{-1} at both frequencies, such that the uncertainty of the RM is smaller than $20\,\mathrm{rad\,m^{-2}}$. The large S/Ns of the images make the uncertainty in RM that small, despite the small difference in λ^2. We also note that the RM is low enough that bandwidth depolarization is negligible. Finally, we employ the RM map to derotate the PA map at 7.4 GHz to obtain the intrinsic B-field direction.

3. Results

Our total intensity maps of G21.5−0.9 at 5 and 7.4 GHz are shown in Figure 1. The PWN has an overall spherical shape. It appears to be more extended at 5 GHz due to the larger beam size and higher surface brightness. The pulsar was not detected. We marked its position in the images using the reported values (R.A., decl. $=18^\mathrm{h}33^\mathrm{m}33\fs57$, $-10°34'07\farcs5$; Camilo et al. 2006). The PWN emission peaks at $12''$ NW of the pulsar. The brightest regions form a double-lobed structure, at about equal distance NW and SE from the pulsar. The double-lobed structure is more obvious at 7.4 GHz because of the better resolution. The two lobes are separated by $\sim16''$. The X-ray torus of G21.5−0.9 ($11\farcs4$ in size) appears to be aligned with the lobes (Figure 1), hinting that they are related. This feature is similar to that reported in previous studies (Furst et al. 1988; Bietenholz & Bartel 2008). Even finer structures of G21.5−0.9 was observed at a higher resolution (Bietenholz & Bartel 2008). We will focus on the polarization results in this paper.

The integrated flux density of G21.5−0.9 is 6.6 ± 0.1 Jy and 6.1 ± 0.1 Jy at 5 and 7.4 GHz, respectively. The uncertainties reported above are mostly systematics estimated by using different source regions. The uncertainties due to calibration and statistical fluctuations are negligible, since the PWN is very bright. The flux density measurements give a spectral index of $\alpha = 0.16 \pm 0.08$ ($S_\nu \propto \nu^{-\alpha}$). We also tried the spectral tomography method (Katz-Stone & Rudnick 1997), and found a similar value and no significant spatial variation in the

spectral index. Our results are consistent with those reported by Bhatnagar et al. (2011), using a slightly different technique.

Figure 2 shows the PI map of the PWN. The PI is low at the center and it peaks near the NW lobe, whereas the polarized emission near the SE lobe is not obvious. The position of the peak of the PI is offset by around $7''$ from the peak of the total intensity. Figure 3 shows the linear polarization fraction map (PF = PI/I) of G21.5−0.9. The overall PF is $\sim13\%$ at both 5 and 7.4 GHz. The PF mainly depends on the magnetic field structure and magnetic turbulence; thus, this map provides different information from the PI map. The PF increases gradually from about zero at the center to $\sim30\%$ near the boundary.

Figure 4 shows the RM map derived from the PA maps at the two bands. The RM values range from $+25$ to $+105\,\mathrm{rad\,m^{-2}}$, with uncertainty less than $20\,\mathrm{rad\,m^{-2}}$. The RM of the nebula near the pulsar position is about $+50\,\mathrm{rad\,m^{-2}}$, which is similar to the $+60\,\mathrm{rad\,m^{-2}}$ measured from the pulsed emission of PSR J1833 −1034 (Serylak et al. 2021). Since the pulsar emission only passes through half of the nebula, its RM value can be different from that of the PWN if the internal Faraday rotation is strong. In Figure 4, we illustrate the spin axis direction of the central pulsar inferred from the X-ray torus (Ng & Romani 2008). The RM map shows a symmetric pattern that aligns with the pulsar spin direction. The RM values are lower along the axis and gradually increase outward. The symmetry can also be seen in the intensity map, but not in the PI map.

We use the RM map to correct for the Faraday rotation. The resulting intrinsic orientation of the B-field vectors (PA + 90°) is plotted in Figure 5. The PA uncertainties in the map are smaller than 4°. We find an overall radial field, as reported in previous works (Becker & Szymkowiak 1981; Reich 2002). In addition, our high-resolution map shows that some magnetic field vectors appear to deviate from the radial direction by at most 45°. The deviation is most evident at the bright double lobes, forming an hourglass-like structure with $\sim30''$ across. Observations with better resolution and at higher sensitivity are needed to confirm this feature.

4. Discussion

4.1. Double-lobed Structure

The double-lobed structure in G21.5−0.9 is also observed in other radio PWNe, including Vela (Dodson et al. 2003),
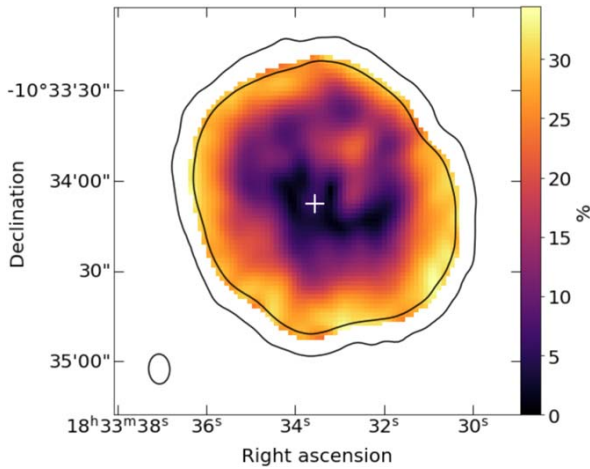
Figure 3. Linear PF of G21.5−0.9 at 7.4 GHz. The map is clipped if the uncertainty is above 1%. The contours represent the 7.4 GHz surface brightness at 1 and 10 mJy beam^{-1}.
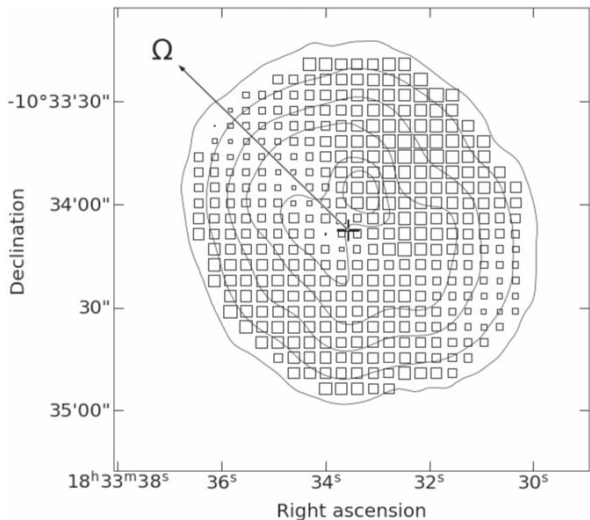

Figure 4. RM of G21.5−0.9. The boxes scale linearly from +25 to +105 rad m^{-2}. The uncertainty is below 20 rad m^{-2}. The contours represent the 7.4 GHz total intensity at 160, 140, 100, 50, 10, and 1 mJy beam^{-1}. The arrow indicates the projected spin axis direction of PSR J1833−1034.

G343.1−2.3 (Romani et al. 2005; Y. H. Liu et al. 2022, in preparation), and G76.9+1.0 (Landecker et al. 1993; Arzoumanian et al. 2011; Arumugasamy et al. 2014). 3C58 (Reich 2002; Bietenholz 2006) and DA 495 (Kothes et al. 2008) show only a double-lobed structure in the polarized emission, but not in the total intensity. The positions of the lobes are always symmetric about the pulsar spin axis, except for DA 495, whose pulsar spin orientation is unknown. The symmetry suggests that the X-ray torus might be related to the lobes. The observed double-lobed morphology of the Vela and G76.9+1.0 PWNe was suggested to result from the toroidal emission region, with specific viewing geometry (Chevalier & Reynolds 2011). This model, however, may not be applicable to spherical PWN like G21.5−0.9.

All these lobes are only seen in radio, suggesting the accumulation of less energetic particles in these regions. It is peculiar that they all show a double-lobed morphology, but not
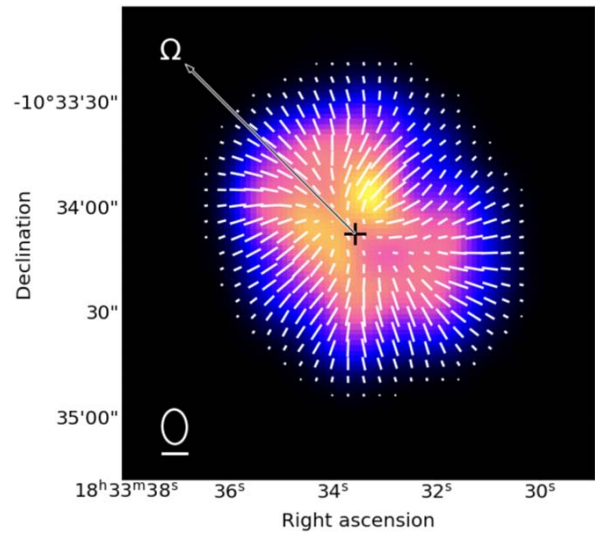

Figure 5. Total intensity map of G21.5−0.9 at 7.4 GHz overlaid with the intrinsic magnetic field orientation. The lengths of the vectors are proportional to the polarized intensity. The black cross indicates the position of PSR J1833−1034. The magnetic field map has a beam size of FWHM 9″9 × 7″0, as indicated by the ellipse at the lower left. The bar below indicates a polarized flux density of 20 mJy beam^{-1}. The vectors are clipped if the uncertainty in the PA is larger than 4°. The arrow shows the projected spin axis direction of PSR J1833−1034 (Ng & Romani 2008).

a ring-like one, as in the X-ray torus. In Table 2, we summarize the properties of four double-lobed radio PWNe. We notice that the two lobes always show different brightness. Vela has the largest peak brightness difference between the two lobes of a factor of 2. There is also a large range in the physical separation of the lobes, from 0.33 pc in G21.5−0.9 to 8.7 pc in G76.9 +1.0. From the table, there seems to be a trend that older PWNe have larger lobe separation. This trend also exists for the ratio of the separation to the size of the X-ray torus. If confirmed, this could imply an outward motion of the lobes.

4.2. Internal Faraday Rotation

It is intriguing that the RM toward G21.5−0.9 appears to show a symmetric pattern about the pulsar spin axis (Figure 4). Instead of the chance alignment of the foreground RM structure, this more likely results from the Faraday rotation within the PWN. This is supported by the amplitude of the RM variation. Minter & Spangler (1996) derived a structure function for the foreground RM, $D_{RM}(\delta\theta)$, in terms of angular scale, due to the fluctuation of both the interstellar electron density and the galactic magnetic field caused by turbulence (see the Appendix for details). The theoretical structure function predicts the average RM difference for a given angular separation. For the case of G21.5−0.9, we obtain $D_{RM}(\delta\theta) \approx (13B_{ran}^2 + 11)\delta\theta^{5/3}$ rad^2 m^{-4}, where B_{ran} is the strength of the random B-field component in units of μG and $\delta\theta$ is the angular separation in units of arcmin. The value of B_{ran} depends on the observation direction, and its largest empirical value is 9 μG (Haverkorn et al. 2008). This model can be compared with our observations, and the result is shown in Figure 6. The structure function is calculated up to an angular scale of 45″, the same as the PWN size. The observed structure function is larger than the theoretical values at all $\delta\theta$ for $B_{ran} \leqslant 9$ μG. This suggests that the foreground Faraday rotation

	G21.5−0.9	Vela	G343.1−2.3	G76.9+1.0
Age (kyr)	0.87	11	18	$9 \sim 40$
Separation between two lobes (pc) (l_{lobes})	0.36	0.36	1.24	8.7
Peak brightness ratio between two lobes	1.07	2	1.14	1.08
Size of X-ray torus (pc) (l_{torus})	0.26	0.06	0.1	⋯
l_{lobes}/l_{torus}	1.4	6	12	⋯
$\dot{E}_{pulsar}$ (10^{36} erg s^{-1})	34	6.9	3.4	30

References. The X-ray torus sizes are from Ng & Romani (2008).

is unable to explain the rapid variation of RM in G21.5−0.9 unless B_{ran} is exceptionally high. This result indicates that the observed RM variation is unlikely to be due to the foreground.

Pulsar wind in general cannot contribute significant Faraday rotation. The main reason is that it consists of electron–positron plasma, such that the Faraday effect is canceled out. Moreover, Faraday rotation is weak for relativistic particles (Jones & Odell 1977), and their number density in pulsar wind is low; for example, less than 10^{-5} cm^{-3} for G21.5−0.9 (Hattori et al. 2020). On the other hand, the RM fluctuation we observed ($\sim$80 rad m^{-2}) can be explained by electrons originating from the SN ejecta. For a magnetic field strength of 130 μG (Guest et al. 2019) and a nebula size of 2 pc, the observed RM value requires an average electron density of $\sim$0.8 cm^{-3}. We have doubled the density to account for the effect of the internal Faraday rotation (Burn 1966). Assuming that G21.5−0.9 is a sphere, the total number of cold electrons can be contributed by 0.1 $M_\odot$ of hydrogen or 0.2 $M_\odot$ of high-Z elements. This is possible for G21.5−0.9, since the swept-up ejecta mass is suggested to be 0.8 $M_\odot$ (Hattori et al. 2020).

In this picture, the spatial variation of the RM is then caused by the variation of either the line-of-sight magnetic field strength or ejecta electron density. The radial B-field of G21.5−0.9 is expected to produce a spherically symmetric RM pattern rather than an axisymmetric one. Also, nonuniform field strength should result in a correlation between the RM and the surface brightness, which is not observed. We therefore conclude that there is an axisymmetric distribution of ejecta electrons about the pulsar spin axis. This could be due to an asymmetric SN explosion or a latitude-dependent mixing process between the pulsar wind and the SN ejecta. Further simulations are needed to understand the details of these processes.

The RM distributions of the Boomerang PWN (Kothes et al. 2006) and CTB 87 (Guest et al. 2020; Kothes et al. 2020) show similar patterns as G21.5−0.9. They are both symmetric about the pulsar spin axis, and the RM values are lower or more negative along the axis. They have also been suggested to be caused by the internal Faraday rotation (Kothes et al. 2006, 2020). Unlike G21.5−0.9, both of them are evolved PWNe that have been crushed by the SN reverse shock. This could imply that the axisymmetric RM pattern already existed before the crush and was not disturbed by the crush. However, we note that these two sources have different B-field structures than G21.5−0.9. The origins of their RM patterns thus may not be the same as for our case.

4.3. Polarization Properties

Our high-resolution polarization map confirms that G21.5−0.9 has a radial magnetic field overall. A previous infrared study found a toroidal field in the inner PWN with scale of 4″
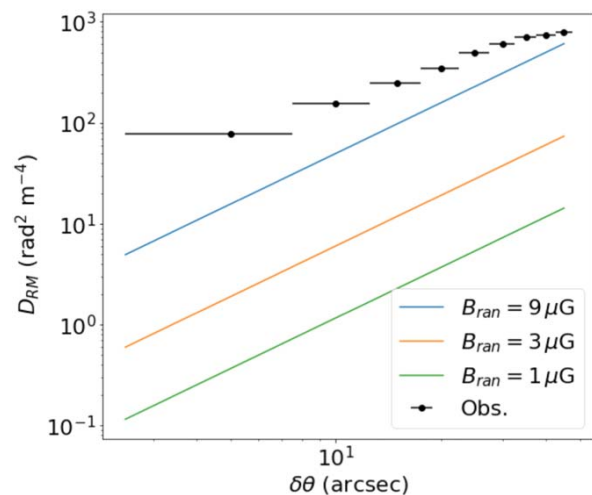

Figure 6. Structure functions of the RM for G21.5−0.9. The black dots are the observational results calculated from the RM map in Figure 4. The colored lines show the theoretical model with different strengths of magnetic fluctuation (Minter & Spangler 1996).

(i.e., 0.1 pc; Zajczyk et al. 2012). If this extends to larger radii, its influence on the inner PWN may explain the hourglass structure seen in the PL map (see Section 3). It is, however, unclear what the extent of the toroidal field is and how it connects to the global radial field of the radio PWN. Nevertheless, as we will show in Section 5 below, we can reject the existence of any large-scale toroidal field components with comparable strength. This suggests that the toroidal field is only important to the inner nebula.

In addition to G21.5−0.9, the Crab Nebula and DA 495 also show radial magnetic field structures. For the Crab, the radial field is only found near the boundary, and it could be caused by fluid instability between the pulsar wind and the ambient medium (Bietenholz & Kronberg 1990). While numerical simulations suggest that the instability layer can be as thick as 30% of the PWN radius (Bucciantini et al. 2004), this is still insufficient to explain our observations. The radial field of DA 495 has been suggested to be a combination of dipole and toroidal fields (Kothes et al. 2008), which is not the case for G21.5−0.9 (see Section 5 below).

Finally, we note that as shown in Figure 3, the PF is very low near the center and gradually increases toward the edge. This cannot be solely due to beam depolarization, since this effect becomes negligible for angular scales beyond the beam size. As an example, consider a radial B-field emitting at 100% PF locally: the PF is zero at the center, because of beam depolarization, but rises to 85% just one beamwidth outside. In

Section 5, we suggest that the radially increasing PF is caused by magnetic field geometry and turbulence. The low PF near the center could also lead to the observed offset between the peaks of the total intensity emission and the polarized emission.

5. Magnetic Field Models

In this section, we aim to construct a simple model to fit the observed total intensity, PF, and magnetic field orientation of G21.5−0.9, so that we can determine the global B-field configuration. We will then employ the best-fit model to study the effects of internal Faraday rotation.

5.1. Model Descriptions

Three-dimensional (3D) simulations have shown that the magnetic field in a PWN could have significant turbulence (Porth et al. 2014). In our model, we consider ordered and disordered (i.e., turbulent) B-field components, and adopt the method of Bandiera & Petruk (2016) to calculate synchrotron emissivity in the presence of small-scale magnetic turbulence. On top of the ordered magnetic field $\boldsymbol{B}$, a Gaussian random field with variance $(|\boldsymbol{B}|\sigma)^2$ in each direction is introduced to account for a turbulent environment. The energy ratio between the ordered and disordered fields is thus $B_{\mathrm{ordered}}^2/B_{\mathrm{disordered}}^2 = 1/3\sigma^2$. A larger σ would decrease the local PF. For simplicity, we assume a constant $\sigma = 0.7$ over the entire nebula. The value was chosen so that the PF values are similar to the observations. This gives $B_{\mathrm{ordered}}/B_{\mathrm{disordered}} \sim 0.8$, which is close to the previous estimate (Furst et al. 1988).

We considered three models for the ordered magnetic field. The first one is a radial B-field in 3D (the R model) motivated by our polarization map. The second one is a toroidal field plus a radial field (the TR model), because the former was observed in the inner PWN (Zajczyk et al. 2012). The third model is a toroidal field plus a dipole field (the TD model), which was used to explain the observations of DA 495 (Kothes et al. 2008). Mathematically, these can be expressed in spherical coordinates (r, θ, ϕ) as

$$\boldsymbol{B_R}(r) = -B_0\hat{r}, \tag{1}$$

$$\boldsymbol{B_{TR}}(r, \theta) = B_0(\sin\theta\hat{\phi} - \hat{r}), \tag{2}$$

and

$$\boldsymbol{B_{TD}}(r, \theta) = B_0\left(\cos\theta\hat{r} + \frac{1}{2}\sin\theta\hat{\theta} + \sin\theta\hat{\phi}\right), \tag{3}$$

where B_0 is a constant to characterize the field strength. The form of the toroidal component in the TR and TD models is adopted from Del Zanna et al. (2006). For simplicity, we consider equal strengths for the radial, toroidal, and dipolar field components. The pulsar spin axis points to the $+z$ direction, and θ is the polar angle measured from the spin axis.

We note that the directions of the radial field (inward or outward) and the toroidal field (clockwise or counterclockwise) are not constrained by the surface brightness map because they give the same synchrotron emissivity. However, they induce different signs of internal Faraday rotation. An outward radial field produces a positive RM and an inward field produces a negative RM. The average RM of G21.5−0.9 is ∼65 rad m^{-2} near the edge and ∼50 rad m^{-2} at the center. This suggests a negative RM contribution by the nebula, hence an inward radial field. The direction of the toroidal field is randomly picked.

Except for the magnetic field configuration, the other settings of the models are the same.

The viewing angle between the pulsar spin axis and the line of sight for G21.5−0.9 is 85°.4 (Ng & Romani 2008). We take it as 90° in the modeling. We consider only the region from the TS ($R_{\mathrm{TS}} = 0.13$ pc) to the outer radius ($R_{\mathrm{pwn}} = 1.14$ pc), and we assume no emission outside this region.

To compute the synchrotron emissivity, we also need to specify the pulsar wind particle distribution. We adopt the diffusion model deduced from the X-ray photon index and TeV brightness profiles (Tang & Chevalier 2012; Abeysekara et al. 2017). For injected particles following a power-law energy distribution, $N(E, r=0) = KE^{-(2\alpha+1)}$, there is an exact formula for the density profile (see Equation (17) in Gratton 1972). When $E \ll 422/(B_0^2 t)$ and $r \ll \sqrt{Dt}$ (in cgs units), this can be approximated by

$$n_{\mathrm{pwn}}(r) \propto \frac{K}{Dr} \quad \text{for} \quad R_{\mathrm{TS}} < r < R_{\mathrm{pwn}}, \tag{4}$$

where D is the diffusion coefficient and t is the age of the PWN. For our case, the first condition is easily satisfied, given that we are dealing with radio-emitting electrons. The diffusion coefficient D is found to be 3.7×10^{27} cm^2 s^{-1} by fitting the X-ray data of G21.5−0.9 (Tang & Chevalier 2012). Although D could be smaller for less relativistic particles, the difference is subtle. Given that the PWN age is 870 yr and the radius is around 1 pc, the second limit is approximately fulfilled. We do not attempt to fit B_0 and K, but arbitrarily set their values and only focus on the relative brightness. The spectral index α is taken to be $+0.16$, derived from our observations.

We followed the recipe derived by Bandiera & Petruk (2016) for deriving synchrotron emission in the Stokes I, Q, and U parameters. The final maps in each Stokes parameter are obtained by integrating the emission along each line of sight. We simulate the emission at 5 GHz, the same as the observations. Absorption and scattering are negligible at this frequency. Finally, we smooth the synthetic emission maps by the same beam size as the observations to allow a direct comparison. As we will show in Section 5.3 below, depolarization caused by internal Faraday rotation is negligible at this frequency. We therefore did not account for this effect in our modeling.

5.2. Synthetic Maps

Figure 7 shows the simulated surface brightness and polarization maps of different magnetic field configurations. When comparing with the observations, we focus on two prominent features: the radial magnetic field structure and the radially increasing PF. The TR model results in an overall radial field structure. However, there are two local minima in the PF map along the polar axis, rather than a minimum at the center. The low-PF regions are where the toroidal and radial fields are perpendicular to each other. The TD model barely reproduces a radial field structure, and the PF map even has four local minima, for the same reason as above. The R model successfully produces a radial field pattern and radially increasing PF.

In Figure 8, we compare the simulated flux density and PF profiles with the observations. It shows that the relative surface brightness is insensitive to the magnetic field structure. The general downward trend is caused by the spherical geometry and the $1/r$ dependence of the pulsar wind particle density. The differences between the B-field configurations are not significant,
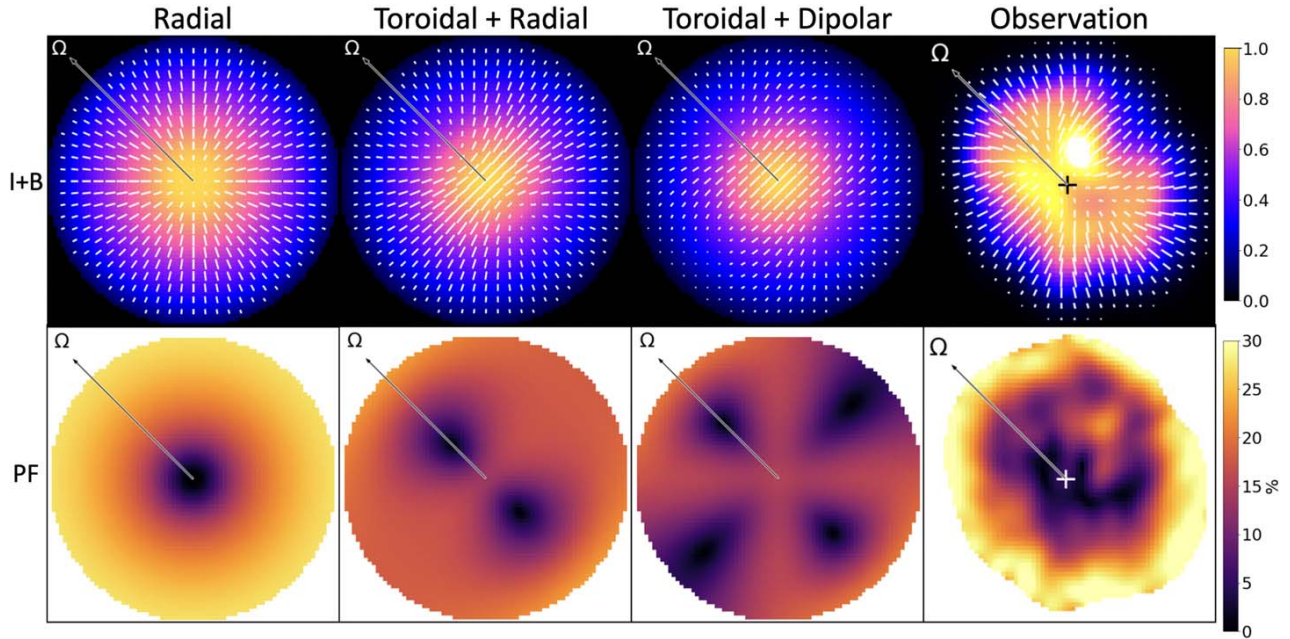
Figure 7. Simulated results of the radial field (R) model, the toroidal plus radial field (TR) model, and the toroidal plus dipolar field (TD) model. The observation results are shown on the right for comparison. The upper row shows the normalized surface brightness overlaid with the magnetic field orientation. The lower row shows the PF maps.

and all are roughly consistent with the observations. Note that our model results are very similar to one with constant particle density and the magnetic field strength decreasing as $1/r$ (Furst et al. 1988). This is due to the degeneracy of these two parameters for synchrotron radiation.

Unlike the brightness maps, different magnetic field configurations give very different PF maps. Only the R model shows an increasing trend with radius that generally matches the observations. We argued in Section 4.3 that the angular size of this trend is too large to be attributed to beam depolarization. The increasing trend can be understood as follows. First, considering the case without turbulence (i.e., $\sigma = 0$), if we ignore the Faraday effect, the observed polarization direction is perpendicular to the orientation of the B-field projected onto the plane of the sky. For the R model, picking any line of sight, the projected B-field always has the same position angle. Therefore, after projection, the polarized emission from all cells in 3D adds up coherently, such that the observed PF is constant over the entire nebula and equal to the intrinsic PF of each cell. Note that this is not the case for the TR and TD models. They are expected to have lower PFs in the inner nebula, due to the changing magnetic field PA along the line of sight.

Now, considering turbulence, an analogous formula of the local PF in each cell can be written as $PF_{\mathrm{local}} \sim \frac{PI \sin \eta}{I (\sin \eta + \sigma)}$, where η is the angle between the line of sight and the magnetic field in 3D. A large turbulence level σ thus leads to a lower PF, and the latter also depends on η. In the R model, the edge of the nebula has $\eta \approx 90°$, and hence the highest PF, while the PF is lowest near the center as $\eta \approx 0$. The same result can be derived rigorously using a full mathematical treatment with the synchrotron recipe (Bandiera & Petruk 2016).

We conclude that the R model is sufficient for explaining the observed radial profiles of brightness and PF. This rules out the existence of a global toroidal or dipolar B-field components with comparable strength to the radial field.
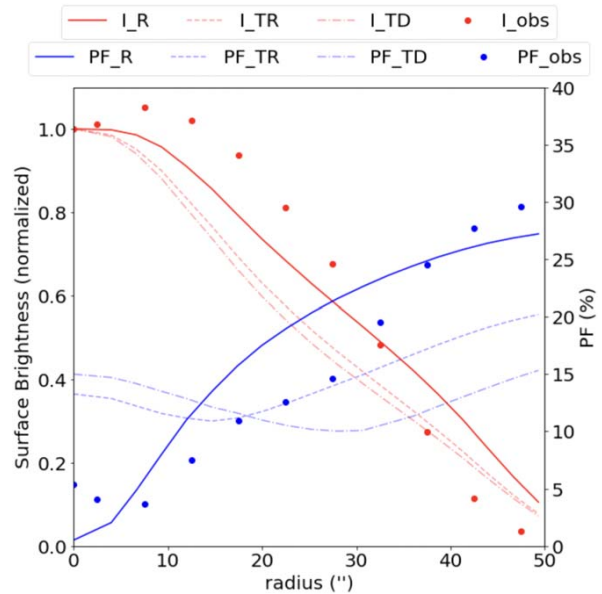

Figure 8. Observed and simulated radial surface brightness and PF profiles of G21.5−0.9. The red curves and dots are the normalized surface brightness. The blue curves and dots are the PF. The solid lines, dashed lines, dashed–dotted lines, and dots represent the R model, the TR model, the TD model, and the observations, respectively.

5.3. Internal Faraday Rotation

In the following discussion, we focus on the R model to discuss its effect on the internal RM and depolarization. We model the ejecta electron density distribution as $n_{\mathrm{sn}}(\theta) = n_{\mathrm{sn},0} |\cos \theta|$, since it fits our observational results, where $n_{\mathrm{sn},0}$ is a constant and θ is
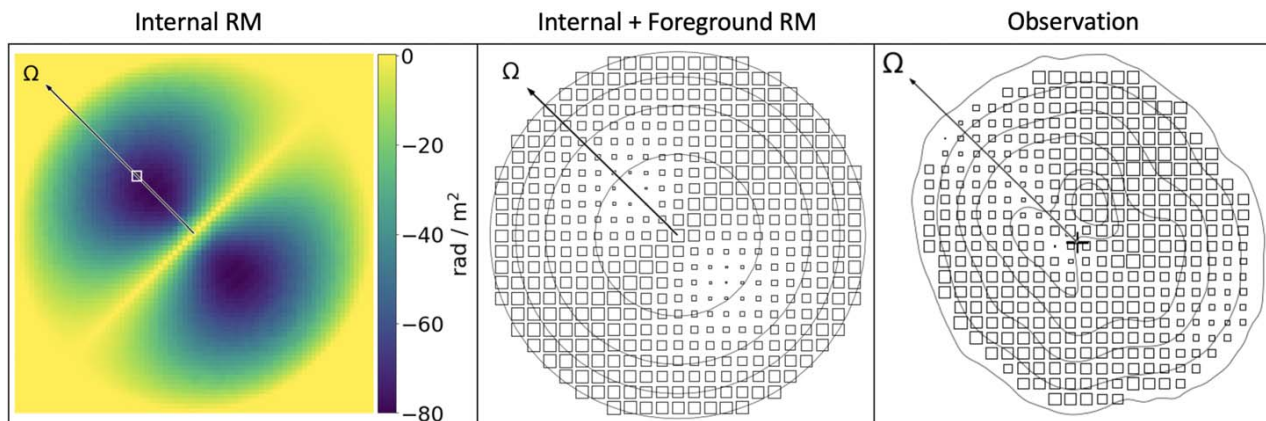
Figure 9. Simulated RM maps at 5 GHz compared with observations. Left: the RM due to internal Faraday rotation. The white box indicates the pixel we used to analyze how the observed values may change with wavelength (see text and Figure 10). Middle: RM map with a foreground RM of 105 rad m^{-2} on top of the internal RM. The scale of the boxes is identical to that for the observations (right panel).

the polar angle measured from the spin axis of the pulsar. These electrons are cold, such that their contribution to the synchrotron emission is negligible. We find that for $B_0 = 130\,\mu$G (Guest et al. 2019), $n_{sn,0} = 4.2$ cm^{-3} can give an RM fluctuation of $\Delta RM = 80$ rad m^{-2} within the PWN. This implies a volume-averaged number density of $\sim 0.5 n_{sn,0} = 2.1$ cm^{-3}.

Figure 9 shows the simulated RM maps. The internal RM values are all nonpositive because the magnetic field in the near hemisphere points away from the observer. There is no Faraday rotation at the equator, since we assumed $n_{sn}(\theta = \pi/2) = 0$ in the model. For a better comparison with the data, we added a constant foreground RM of 105 rad m^{-2}. The resulting RM map is shown in the middle panel of Figure 9. The RM values are smaller along the pulsar spin axis, which generally matches with the observations. At the PWN boundary, our model suggests minimal internal Faraday rotation due to the short light path. This gives a nearly constant RM value around the boundary, in contrast to what we have observed. The discrepancy could be an observational bias, since some pixels near the edge are clipped in the map due to the low surface brightness.

Internal Faraday rotation can lead to depolarization and break the linear relation between PA and λ^2 at low frequency (Burn 1966). This has been suggested to be the cause of the frequency-dependent depolarization found in the Boomerang and CTB 87 PWN (Kothes et al. 2006, 2020). We illustrate this effect with a line of sight near the strongest internal RM (see the left panel of Figure 9). We calculated the Faraday rotation of the emission from different depths, then summed the rotated Stokes Q and U parameters respectively to determine the resulting PA and PF. This calculation was repeated for different wavelengths, and the results are plotted in Figure 10. We found that the PA varies linearly with λ^2 at short wavelengths, but starts to deviate significantly at frequencies $\lesssim 2$ GHz. For the PF, it drops continuously as the wavelength increases, and reaches half of its maximum value at ~ 2 GHz. Our result suggests that the internal Faraday effects on the PA and PF are minimal at our observation frequency, but could be significant in the L band. For instance, we cannot simply derive the intrinsic PA using a single RM value, but need to combine it with higher-frequency (e.g., C-band) data to solve for the
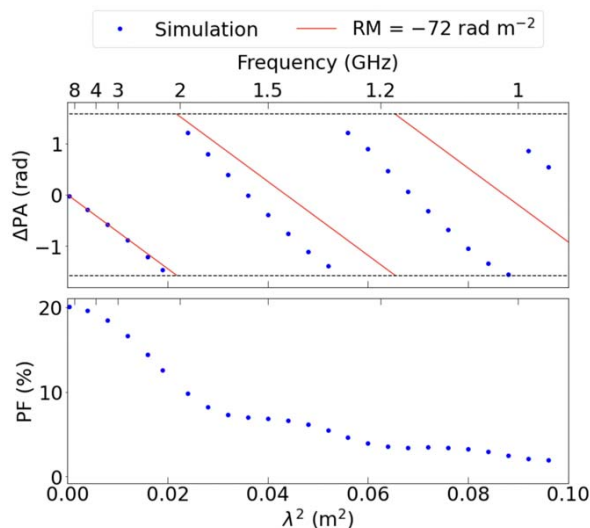

Figure 10. Illustration of the PA change and PF with respect to wavelength for the pixel indicated in Figure 9. The blue dots show the simulated results and the red lines indicate a single RM value of -72 rad m^{-2}, obtained by fitting the PA at short wavelengths (top panel).

Faraday dispersion function using RM synthesis (Brentjens & de Bruyn 2005).

6. Conclusion

We present a polarimetric study of the PWN G21.5−0.9 using archival C-band VLA data, and construct a simple magnetic field model to explain the observations. Our main discovery and conclusions are summarized below.

This is the first time that the RM map of G21.5−0.9 has been obtained. We found a symmetric structure about the pulsar spin axis, suggesting significant Faraday rotation within the PWN. We suggest that this is due to electrons from the SN ejecta instead of pulsar wind. In addition, the spatial variation of the RM is more likely to be caused by nonuniformly distributed ejecta electrons, rather than by the variation of the magnetic field. Such nonuniform distribution could be the result of

asymmetric SN explosion or a latitude-dependent mixing process between the pulsar wind and the ejecta.

Our polarization results reveal a global radial magnetic field for G21.5−0.9. We constructed a simple model with a radial field plus small-scale turbulence and showed that it can generally reproduce the observed surface brightness and PF maps. The magnetic turbulence is important in explaining the radially increasing PF.

The upcoming X-ray polarimeters, including the IXPE (Weisskopf et al. 2016), the XIPE (Soffitta et al. 2013), and the eXTP (Zhang et al. 2019), can provide complementary information about the magnetic field configuration of G21.5−0.9.

Appendix
RM Structure Function

The RM structure function is defined as $D_{\mathrm{RM}}(\delta\theta) = \langle [\mathrm{RM}(\theta) - \mathrm{RM}(\theta + \delta\theta)]^2 \rangle_\theta$, where θ is the observing position, $\delta\theta$ is the angular separation, and $\langle \rangle_\theta$ means the average over all possible positions of θ. We aim to find a theoretical structure function that is applicable to G21.5−0.9. Minter & Spangler (1996) derived the RM structure function based on the Kolmogorov turbulence model:

$$
\begin{aligned}
D_{\mathrm{RM}}(\delta\theta) = & \left\{ 251.226 \left[\left(\frac{n_e}{0.1 \ \mathrm{cm}^{-3}} \right)^2 \left(\frac{C_B^2}{10^{-13} \ \mathrm{m}^{-2/3} \ \mu\mathrm{G}^2} \right) \right. \right. \\
& \left. + \left(\frac{B_\parallel}{\mu\mathrm{G}} \right)^2 \left(\frac{C_n^2}{10^{-3} \ \mathrm{m}^{-20/3}} \right) \right] \\
& + 23.043 \left(\frac{C_n^2}{10^{-3} \ \mathrm{m}^{-20/3}} \right) \\
& \times \left(\frac{C_B^2}{10^{-13} \ \mathrm{m}^{-2/3} \ \mu\mathrm{G}^2} \right) \left(\frac{l_0}{\mathrm{pc}} \right)^{2/3} \right\} \\
& \times \left(\frac{L}{\mathrm{kpc}} \right)^{8/3} \left(\frac{\delta\theta}{\mathrm{deg}} \right)^{5/3},
\end{aligned}
\tag{A1}
$$

where n_e is the mean electron density, $B_\parallel$ is the mean magnetic field strength of the line-of-sight component, l_0 is the outer scale of the Kolmogorov turbulence, L is the distance to the target, and C_n^2 and C_B^2 indicate the levels of the fluctuations. In particular, $C_B^2 = 5.2 B_{\mathrm{ran}}^2 (l_0)^{-2/3} \times 10^{-13} \ \mu\mathrm{G}^2 \ \mathrm{m}^{-2/3}$, where B_{ran} is the strength of the random B-field. Based on the observed dispersion measure $\mathrm{DM} \approx n_e L = 170 \ \mathrm{pc} \ \mathrm{cm}^{-3}$ (Camilo et al. 2006), $\mathrm{RM} \approx 0.81 n_e B_\parallel L = 110 \ \mathrm{rad} \ \mathrm{m}^{-2}$, and distance $L = 4.7 \ \mathrm{kpc}$ of G21.5−0.9, we estimate that $n_e = 0.036 \ \mathrm{cm}^{-3}$ and $B_\parallel = 0.8 \ \mu\mathrm{G}$. For l_0 and C_n^2, we adopt their values from Minter & Spangler (1996), and note that these are insensitive to our final result. Finally, B_{ran} may take a wide range, from $1 \ \mu\mathrm{G}$ (Minter & Spangler 1996)

Table 3
Input Parameters of D_{RM}

n_e (cm^{-3})	0.036
$B_\parallel$ (μG)	0.8
L (kpc)	4.7
l_0 (pc)	3.6
C_n^2 (10^{-3} m$^{-20/3}$)	1
C_B^2 (10^{-13} m$^{-2/3}$ μG^2)	$2.2 \sim 180$
B_{ran} (μG)	$1 \sim 9$

to $9 \ \mu\mathrm{G}$ (Haverkorn et al. 2008), so we leave it as a free parameter. All these values are listed in Table 3. We stress that these are likely overestimates, since our goal is to derive an upper limit of the theoretical RM fluctuation. Putting these together, the final structure function is then:

$$
D_{\mathrm{RM}}(\delta\theta) \approx \left[13 \left(\frac{B_{\mathrm{ran}}}{\mu\mathrm{G}} \right)^2 + 11 \right] \left(\frac{\delta\theta}{1'} \right)^{5/3} \ \mathrm{rad}^2 \ \mathrm{m}^{-4}. \tag{A2}
$$

ORCID iDs

Paul C. W. Lai ⓘ https://orcid.org/0000-0003-3601-5127
C.-Y. Ng ⓘ https://orcid.org/0000-0002-5847-2612
Niccolo' Bucciantini ⓘ https://orcid.org/0000-0002-8848-1392

References

Abeysekara, A. U., Albert, A., Alfaro, R., et al. 2017, Sci, 358, 911
Amato, E. 2020, arXiv:2001.04442
Arumugasamy, P., Pavlov, G. G., & Kargaltsev, O. 2014, ApJ, 790, 103
Arzoumanian, Z., Gotthelf, E. V., Ransom, S. M., et al. 2011, ApJ, 739, 39
Bandiera, R., & Petruk, O. 2016, MNRAS, 459, 178
Becker, R. H., & Szymkowiak, A. E. 1981, ApJL, 248, L23
Bhatnagar, S., Rau, U., Green, D. A., & Rupen, M. P. 2011, ApJL, 739, L20
Bietenholz, M. F. 2006, ApJ, 645, 1180
Bietenholz, M. F., & Bartel, N. 2008, MNRAS, 386, 1411
Bietenholz, M. F., & Kronberg, P. P. 1990, ApJL, 357, L13
Bogovalov, S. V., & Khangoulyan, D. V. 2002, AstL, 28, 373
Brentjens, M. A., & de Bruyn, A. G. 2005, A&A, 441, 1217
Burn, B. J. 1966, MNRAS, 133, 67
Camilo, F., Ransom, S. M., Gaensler, B. M., et al. 2006, ApJ, 637, 456
Chevalier, R. A., & Reynolds, S. P. 2011, ApJL, 740, L26
Contopoulos, I., Kazanas, D., & Fendt, C. 1999, ApJ, 511, 351
Del Zanna, L., Volpi, D., Amato, E., & Bucciantini, N. 2006, A&A, 453, 621
Dodson, R., Lewis, D., McConnell, D., & Deshpande, A. A. 2003, MNRAS, 343, 116
Furst, E., Handa, T., Morita, K., et al. 1988, PASJ, 40, 347
Gaensler, B. M., & Wallace, B. J. 2003, ApJ, 594, 326
Gratton, L. 1972, Ap&SS, 16, 81
Guest, B., Safi-Harb, S., MacMaster, A., et al. 2020, MNRAS, 491, 3013
Guest, B. T., Safi-Harb, S., & Tang, X. 2019, MNRAS, 482, 1031
Gupta, Y., Mitra, D., Green, D. A., & Acharyya, A. 2005, CSci, 89, 853
Hattori, S., Straal, S. M., Zhang, E., et al. 2020, ApJ, 904, 32
Haverkorn, M., Brown, J. C., Gaensler, B. M., & McClure-Griffiths, N. M. 2008, ApJ, 680, 362
Johnston, S., McClure-Griffiths, N. M., & Koribalski, B. 2004, MNRAS, 348, L19
Jones, T. W., & Odell, S. L. 1977, ApJ, 214, 522
Katz-Stone, D. M., & Rudnick, L. 1997, ApJ, 488, 146
Kothes, R., Landecker, T. L., Reich, W., Safi-Harb, S., & Arzoumanian, Z. 2008, ApJ, 687, 516
Kothes, R., Reich, W., Safi-Harb, S., et al. 2020, MNRAS, 496, 723
Kothes, R., Reich, W., & Uyanıker, B. 2006, ApJ, 638, 225
Landecker, T. L., Higgs, L. A., & Wendker, H. J. 1993, A&A, 276, 522
Matheson, H., & Safi-Harb, S. 2010, ApJ, 724, 572

McMullin, J. P., Waters, B., Schiebel, D., Young, W., & Golap, K. 2007, in ASP Conf. Ser. 376, Astronomical Data Analysis Software and Systems XVI, ed. R. A. Shaw, F. Hill, & D. J. Bell (San Francisco, CA: ASP), 127
Minter, A. H., & Spangler, S. R. 1996, ApJ, 458, 194
Moran, P., Shearer, A., Mignani, R. P., et al. 2013, MNRAS, 433, 2564
Ng, C. Y., & Romani, R. W. 2004, ApJ, 601, 479
Ng, C. Y., & Romani, R. W. 2008, ApJ, 673, 411
Porth, O., Komissarov, S. S., & Keppens, R. 2014, MNRAS, 438, 278
Reich, W. 2002, in Proc. 270. WE-Heraeus Seminar on Neutron Stars, Pulsars, and Supernova Remnants, ed. W. Becker, H. Lesch, & J. Trümper (Garching bei München: Max-Plank-Institut für extraterrestrische Physik), 1

Reynolds, S. P., Borkowski, K. J., & Gwynne, P. H. 2018, ApJ, 856, 133
Romani, R. W., Ng, C. Y., Dodson, R., & Brisken, W. 2005, ApJ, 631, 480
Serylak, M., Johnston, S., Kramer, M., et al. 2021, MNRAS, 505, 4483
Soffitta, P., Barcons, X., Bellazzini, R., et al. 2013, ExA, 36, 523
Sun, X. H., Reich, P., Reich, W., et al. 2011, A&A, 536, A83
Tang, X., & Chevalier, R. A. 2012, ApJ, 752, 83
Wardle, J. F. C., & Kronberg, P. P. 1974, ApJ, 194, 249
Weisskopf, M. C., Ramsey, B., O'Dell, S., et al. 2016, Proc. SPIE, 9905, 990517
Zajczyk, A., Gallant, Y. A., Slane, P., et al. 2012, A&A, 542, A12
Zhang, S., Santangelo, A., Feroci, M., et al. 2019, SCPMA, 62, 29502